PAPER • **OPEN ACCESS**

Elucidating the origin of laser-induced nonlinearities in propagation inside transparent media: a comparative numerical study of silicon and fused silica

To cite this article: Amlan Das and Xiaoming Yu 2024 *J. Phys. Photonics* **6** 045016

Journal of Physics: Photonics

PAPER

Elucidating the origin of laser-induced nonlinearities in propagation inside transparent media: a comparative numerical study of silicon and fused silica

Amlan Das[1,2] and Xiaoming Yu[1,*]

[1] CREOL, The College of Optics and Photonics, University of Central Florida, Orlando, FL 32816, United States of America
[2] Centre for Functional Materials, Vellore Institute of Technology, Vellore, Tamil Nadu 632014, India
[*] Author to whom any correspondence should be addressed.

E-mail: yux@creol.ucf.edu and amlandas02@gmail.com

Keywords: silicon, fused silica, self-focusing, pulse-splitting

Supplementary material for this article is available online

OPEN ACCESS

RECEIVED
4 April 2024

REVISED
10 September 2024

ACCEPTED FOR PUBLICATION
18 September 2024

PUBLISHED
7 October 2024

Abstract

The creation of localized bulk modification using femtosecond pulses inside semiconductors like silicon (Si) is quite challenging, whereas it is not difficult to achieve it for dielectric materials like fused silica (FS). This report addresses the fundamental origin of this issue. By taking a simple numerical approach, it has been found that in FS we can deliver stronger fluence due to self-focusing at higher power levels compared to Si. The origin for the above lies in the spatio-temporal pulse-splitting behavior, which is dominant in the case of FS at the focus, whereas, for Si, it is only effective after focus. We have also considered the influence of plasma and Kerr terms to elucidate the reason behind these nonlinearities. For the FS case, omission of Kerr term dominates, whereas, for Si, the influence of each term does not significantly create self-focusing like FS under a similar focusing condition. This study could provide an important guideline for researchers to understand the complexity of laser-matter interaction in transparent materials specifically being studied by many laser-processing industries.

1. Introduction

Direct laser writing inside transparent materials [1–4] is useful in various applications including microfluidics [5], photonics [6] and microelectronics [7] due to its capability of creating 3D structures directly in the bulk. These 3D structures have been fabricated inside many materials such as dielectrics [8–10], semiconductors [11–13], etc. Among them, fused silica (FS) and silicon (Si) are two common materials that have been studied in various fields [14–19].

Generally, FS being transparent from visible to near-infrared wavelengths, where most ultrafast lasers are operational, requires femtosecond laser pulses to create bulk modification conditions inside the material [20–23]. Whereas, Si requires wavelengths longer than $\sim$1.1 μm to become transparent, where internal modification with femtosecond lasers is particularly challenging to achieve [24–26]. However, longer pulse durations [17, 26–28] and other temporal pulse engineering techniques [29, 30] can achieve such modification. Recently, Margaux *et al* [25] have studied that in the shortest (femtosecond) pulse case, the beam is depleted at the pre-focal position due to many nonlinear effects in propagation under strong focusing conditions, so that very low energy is delivered to the focus, which is not sufficient for creating modifications at the focus.

However, internal modification in these materials not only depends on the temporal part of the pulse but also on various other laser parameters (wavelength, focusing conditions, repetition rate, etc) and material properties (band gap, linear/nonlinear refractive index, etc). Therefore, a detailed comparison between these two materials with femtosecond laser pulses under similar focusing conditions is needed to understand the

complex interplay between the processes that have been involved in laser-matter interactions, which can contribute to bulk modification.

The goal of this study is to unveil the associated challenges with the above femtosecond laser processing of transparent materials like Si and FS, as discussed here. We achieve this by performing numerical simulations of nonlinear beam propagation inside FS and Si to study the evolution of beam propagation where pulse energy is taken as the main laser parameter variable under similar focal spot size. Two common wavelengths, 800 and 1500 nm, are chosen for irradiation of FS and Si, respectively. We study the spatial and temporal evolution of the laser field laser-induced plasma and their interactions, which elucidates the origin of strong filamentation in FS and its absence in Si. This study provides a guideline to understand the challenges associated with modifications using different optical material engineering techniques.

2. Model and simulation method

We model an axially-symmetric linearly polarized electric field $E(r,Z,t)= \mathrm{e}_x\,(A(r,Z,t)\,\mathrm{e}^{\mathrm{i}(\beta(\omega)Z-\omega t)}+c.c.)$ propagating along the Z-axis with polarization on the x-axis at optical frequency ω. The envelope $A(r,t)$ describes a femtosecond laser pulse with a Gaussian spatial and temporal profile at $Z=0$. We use the slowly varying envelope approximation in the simulation for 250 fs pulse duration. The following two equations are solved numerically using a solver 'SNOPROP' [31]:

$$2ik\frac{\partial A}{\partial Z}+\frac{\partial^2 A}{\partial r^2}+\frac{1}{r}\frac{\partial A}{\partial r}-k\beta''\frac{\partial^2 A}{\partial \tau^2}-\frac{N_e e^2}{m_e\varepsilon_0 c^2}\left(1-\frac{i\nu_e}{\omega}\right)A+\frac{3\omega}{c^2}\chi|A|^2A+\frac{i\omega}{2c^2}\frac{U_i}{|A|^2}N_0\nu_{MPI}A=0, \quad (1)$$

$$\frac{\delta N_e}{\delta t}=\nu_{MPI}N_0+\nu_i N_e-\eta N_e. \quad (2)$$

Equation (1) is the nonlinear Schrodinger equation for calculating the field envelope A(r, Z, t) [32] where $k=2\pi n_L/\lambda_0=\mathrm{n}_L\omega/c$ is the wavenumber, β'' is the group velocity dispersion, τ is the retarded time variable t-z/v_g with which the reference frame moves at the group velocity v_g, N_e is the density of laser-excited free electrons (solid-state plasma), ν_e is the electron collision frequency, $\chi=4n_{NL}n^2{}_L\varepsilon_0 c/3$ is the real part Kerr nonlinear susceptibility, U_i is the ionization potential, N_0 is atom density and ν_{MPI} is the multiphoton ionization frequency calculated from the Keldysh model. The first four terms in equation (1) describe linear propagation effects that include phase change of propagating along the optical axis, diffraction (second and third terms) and group velocity dispersion, respectively. The fifth term is the nonlinear plasma effects including plasma defocusing and energy loss due to plasma absorption. The sixth term is Kerr self-focusing. The last term is the energy loss due to multiphoton ionization. Equation (2) is the rate equation for calculating carrier density N_e that accounts for multiphoton ionization, impact ionization and recombination, respectively [33, 34]. To obtain multiphoton ionization frequency ν_{MPI}, we use the following relationship [34]:

$$\nu_{MPI}=\frac{2\pi}{(l-1)!}\omega\left(\frac{I}{I_{MPI}}\right)^l, \quad (3)$$

where l is the order of multiphoton absorption ($l=6$ for FS and 2 for Si), and I_{MPI} is the ionization threshold obtained by fitting the Keldysh ionization rate as a function of laser intensity I (figure S1, supplementary materials (SM)). Here, the collision cross-section σ_c is used to calculate the electron collision frequency ($\upsilon_e=(e\sqrt{2}/m_e)\times(A/\omega_L)\times N_0\sigma_c$)) and avalanche ionization rate ($\upsilon_i=(\upsilon_e/U_i)\times(2\times10^2/m_e)\times(|A|^2/\omega^2{}_L)$), respectively.

In this solver, the stimulated Raman scattering terms are removed and only the 'pump' beam (A (r, Z, t) in our case) is retained. Parameters used in this simulation, given in table 1, which are consistent with previous reports [32, 35–41]. We use a total grid size of 6000 × 2000 × 200 ($Z\times r\times t$) with a step size of 1 μm × 0.05 μm × 16 fs (dZ × dr × dt). Convergence of the solution is determined by gradually reducing the step size until the simulation produces nearly identical results. The final grid size and step size are determined by a balance between simulation accuracy and speed. We vary the incident laser power $P_{in}=E_p/\tau_0$ by changing the pulse energy E_p and normalizing P_{in} compared to the critical power for self-focusing $P_{cr}=3.72\lambda_0{}^2/8\pi n_L n_{NL}$ [42]. Here, we vary the ratio P_{in}/P_{cr} from 0.1 to 10 to cover different regimes (linear, nonlinear, strong nonlinear).

Table 1. Basic laser and material's physical parameters, which are considered for this simulation. Here, NA_{eff} is calculated by taking account of refractive index (n) with the following relation ($n \times \sin\theta$) where θ is the focusing angle. W_0 and Z_R are calculated by the following relations: $\lambda/n\pi\theta$ and $n\pi w_0^2/\lambda$, respectively.

Property	Parameter	Quantity		Unit
Constant	Speed of light in vacuum (c)	3×10^8		m s^{-1}
	SI vacuum permittivity (ε_0)	8.854×10^{12}		F m^{-1}
	Electronic charge (e)	1.6×10^{-19}		C
	Mass of electron (m_e)	9.1×10^{-31}		kg
	Reduced Planck's constant ($\hbar$)	1.0546×10^{-34}		J.s
		Fused Silica	Silicon	
Laser	Wavelength in vacuum (λ_0)	800	1500	nm
	Pulse duration FWHM (τ_0)	250	250	fs
	Focal spot $1/e^2$ radius (w_0)	5.3	4.1	μm
	Rayleigh length (Z_R)	159	123	μm
	Effective numerical aperture (NA_{eff})	≈0.047	≈0.115	
Material	Linear refractive index (n_L)	≈1.45 [35]	≈3.48 [36]	
	Nonlinear refractive index (n_{NL})	3.5×10^{-20} [32, 37]	5×10^{-18} [38]	m^2 W^{-1}
	Group velocity dispersion (β'')	36 [32, 35]	1177 [39]	fs^2 mm^{-1}
	Ionization potential energy (U_i)	9 [32]	1.1 [40]	eV
	Multiphoton ionization order (l)	6	2	
	Atomic carrier density (N_0)	2.2×10^{22} [32]	5×10^{22} [40]	cm^{-3}
	Multi-photon intensity (I_{MPI})	8.3×10^{17}	7.4×10^{17}	W m^{-2}
	Electron collision cross-section (σ_c)	1.55×10^{16} [32]	2×10^{16} [41]	cm^2
	Electron relaxation/loss rate (η)	6.7×10^{12} [32]	10^{12} [40]	s^{-1}
	Critical power for self-focusing (P_{cr})	≈1800	≈20	kW

3. Results and discussions

3.1. Laser fluence and plasma density in the focal region

First, we study the laser fluence and excited carrier (N_e) distribution for FS in the focal region. Three power levels ($P_{in}/P_{cr} = 0.1$, 1 and 2) are taken into consideration where the incident power (P_{in}) is far below, equal to and just above the critical power for self-focusing (P_{cr}). When $P_{in}/P_{cr} = 0.1$ for FS, a symmetric distribution of the radial part (r) of our pulse profile along the propagation axis (Z) is observed implying a negligible influence of nonlinear terms on propagation, as shown in figure 1(a). Similarly, the resulting maximum N_e (figure 1(d)) is located near the geometrical focus where the beam is still in the middle of the Rayleigh region (between the two dotted white lines). At the critical power $P_{in} = P_{cr}$, we approach the self-focusing condition [32, 42, 43]. As a result, the delivered plasma has a smaller size, as shown in figure 1(b), whereas the location of maximum N_e is delocalized from geometrical focus but stays within the Rayleigh region (in figure 1(e)). If we further increase the power by a factor of 2 above P_{cr}, we expect strong delocalization of the beam due to strong self-focusing, which can create multiple foci in the propagation direction [44], which are signatures of the beginning of filamentation. In figure 1(c), we have observed two foci where one focus is near the geometric focal position at the $P_{in}/P_{cr} = 2$ case, whereas the second focus is delocalized towards the pre-focal direction ($Z < 3$ mm). The following phenomenon helps to delocalize the dense plasma out of the focal volume (away from geometrical focus), which is shown in figure 1(f). This implies that such long filaments are possible when there are strong asymmetries in the propagation aspect, which has also being observed in previous reports [32, 37, 45, 46].

Whereas in the Si case, at low power level ($P_{in} = 0.1P_{cr}$) maximum fluence is delivered near the geometrical focus where the fluence distribution is no longer symmetric after focus ($Z > 3.1$ mm), as shown in figure 2(a). This implies that at lower power level the nonlinear terms (plasma and Kerr) might play a significant role in the propagation aspect, unlike FS, as discussed before. Similarly, maximum N_e is delivered near geometrical focus (Z_0) at the above same power level, which is shown in figure 2(d). Later, at self-focusing condition (P_{cr}), both maximum fluence (as shown in figure 2(b)) and N_e (in figure 2(e)) are delivered near the focus, even if we find some asymmetric distribution of radial profiles of laser pulses along propagation. When P_{in} is attained in $2P_{cr}$, nonlinear processes, such as filamentation, plasma delocalization, etc, are absent in our simulated 2D profiles by checking both fluence and carrier density evolution, as shown in figures 2(c) and (f), respectively. This is quite the opposite to the FS case, as discussed before.

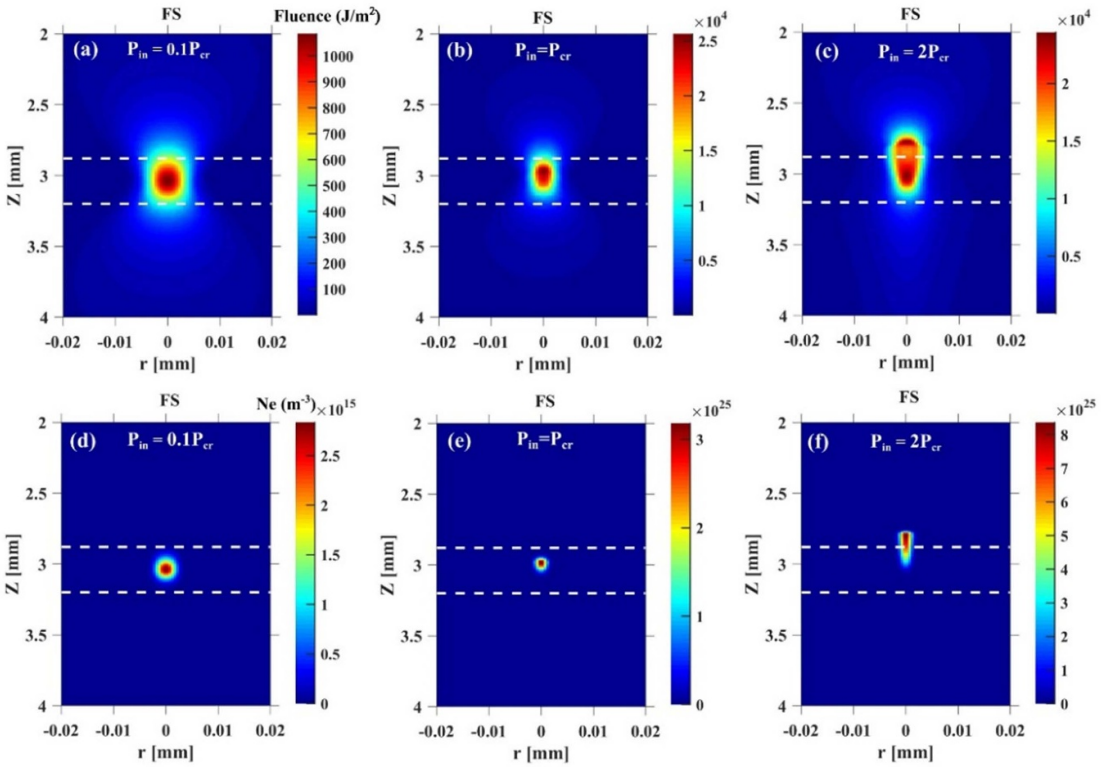

Figure 1. 2D profile of fluence delivery conditions inside FS at three different power levels: $P_{in}/P_{cr} = 0.1$ (a), $P_{in}/P_{cr} = 1$ (b) and $P_{in}/P_{cr} = 2$ (c). Corresponding carrier density evolution profiles are shown at $P_{in}/P_{cr} = 0.1$ (d), $P_{in}/P_{cr} = 1$ (e) and $P_{in}/P_{cr} = 2$ (f). *X*-axis symbolizes the radial profile of the given laser pulse and *Y*-axis suggests the different *Z*-points. Color map shows the local delivered fluence (J m^{-2}) values. White dotted lines address the Rayleigh-point of the laser pulse at a given focusing condition. Geometrical focal position for FS is at $Z_0 = 3.04$ mm.

3.2. Maximum local fluence and carrier density as functions of incident power P_{in}

To understand the above observational differences between FS and Si, we quantitatively study the maximum delivered local fluence and carrier density (N_e) at the focal position (Z_0) in respective of incident power P_{in}, as shown in figure 3. These are extracted by integrating the fluence and N_e distribution at the center of the radial pulse profile ($r = 0$) (See figure S2 in the SM for one example where the $P_{in}/P_{cr} = 2$ case is taken).

In figure 3(a) for FS, the simulated maximum local fluence at $P_{in}/P_{cr} = 0.1$ overlaps the theoretical value (blue dashed line) suggesting little influence of nonlinearities. Note that here the theoretical value signifies the delivered local peak fluence ($2E/\pi\omega^2{}_0$) at the geometrical focal point. As P_{in} increases, deviation from the theoretical value starts to appear. Local fluence reaches the maximum value at $P_{in} = P_{cr}$. If we further increase P_{in}, there is no significant increase of fluence where 'saturation' is achieved by about 2×10^4 J m^{-2}. In our case, the plasma delocalization/filamentation could be one of the reasons for saturation, as discussed before. Whereas, for Si, the maximum local fluence is already below the theoretical value, even at $P_{in} = 0.1P_{cr}$. The deviation with respect to the theoretical value increases with higher P_{in}. There is no obvious 'turning point' (highest local fluence delivery after which deviation is visible) for saturation in the Si case within the $0.1P_{cr}$ to $10P_{cr}$ range. This is quite the opposite to the FS case where we have found reduced fluence delivery conditions.

We show similar curves for the local maximum N_e at Z_0, as shown in figure 3(b). For FS, the local N_e value quickly reaches the maximum and saturation level at P_{cr}, whereas for Si there is no obvious saturation point in this current window of power levels ($P_{in}/P_{cr} = 0.1$ to 10). N_e can reach 10^{26} m^{-3} for FS and 10^{25} m^{-3} for Si. While the observed saturation N_e number for FS (near 10^{26} m^{-3}) is well below the critical plasma density, it has been observed from a previous report [44] that permanent bulk modification (formation of cracks in filament forms in the pre-focal zone) can be reached under similar focusing conditions for 120 fs laser pulse due to filamentation. Whereas for Si, it is very difficult to achieve bulk modification for femtosecond pulses under this given focusing condition. Previous efforts [13, 26] have been made using strong focusing conditions but this is not useful for creating permanent damage. This implies that reaching a critical carrier density does not necessarily influence the bulk damage inside materials. Therefore, other criteria, such as analyzing the deposited energy density of laser pulse at the focus of crossover of the latent heat of fusion of material with experimental evidence, could be taken into generic

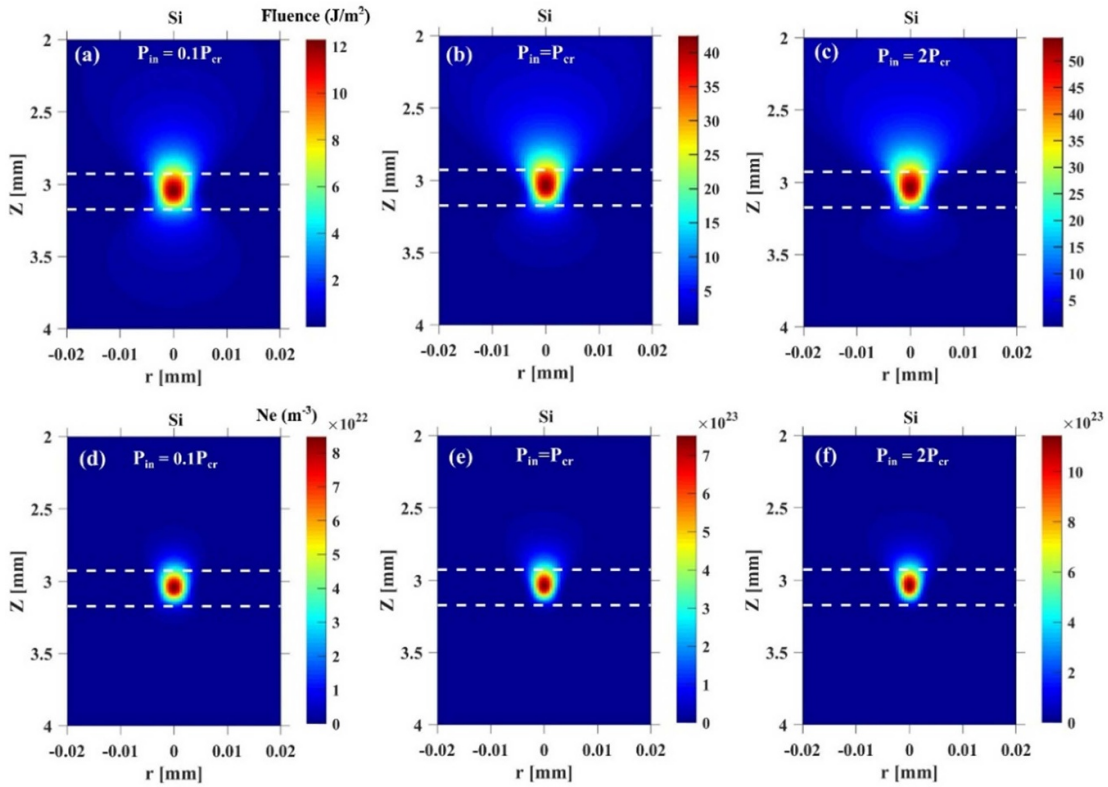

Figure 2. 2D profile of fluence delivery conditions inside Si at three different power levels: $P_{in}/P_{cr} = 0.1$ (a), $P_{in}/P_{cr} = 1$ (b) and $P_{in}/P_{cr} = 2$ (c). Corresponding carrier density (N_e) evolution profiles are shown at $P_{in}/P_{cr} = 0.1$ (d), $P_{in}/P_{cr} = 1$ (e) and $P_{in}/P_{cr} = 2$ (f). Geometrical focal position for Si is at $Z_0 = 3.05$ mm

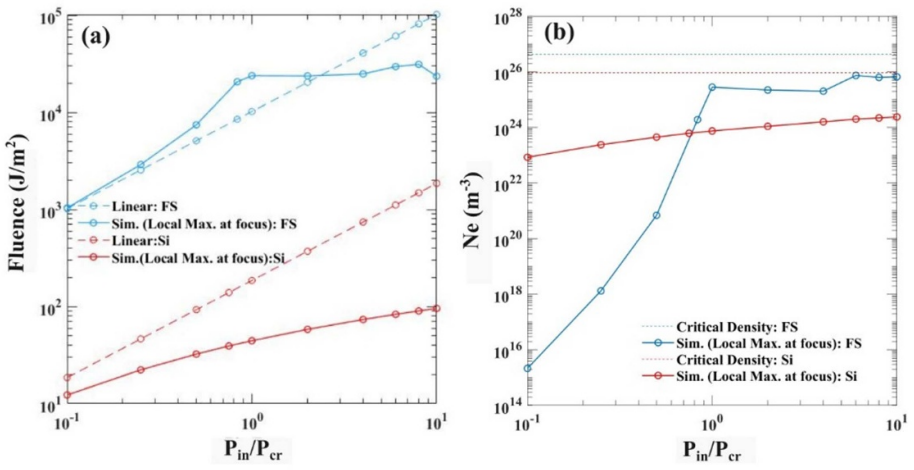

Figure 3. Extracted local fluence (a) and N_e (b) value at different power levels for FS and Si. 'Linear' suggests the propagation condition in the theoretical case. Here, critical density is calculated by the relation: ε_0/e^2 where m_e^* (0.8 and $0.2m_e$ for FS and Si, respectively) and w_l are effective mass and laser frequency, respectively. For FS and Si, the above value is 4.2×10^{26} m^{-3} (similar to previous reports [31, 37]) and 9.5×10^{25} m^{-3}, respectively.

consideration, which has being studied for Si in previous reports [47, 48]. However, at the current stage, the following study is beyond the scope of this study.

3.3. Spatio-temporal pulse profile evolution

In order to understand the origin of strong saturation for FS and no obvious saturation for Si, we have considered the spatial and temporal evolution of simulated pulse in terms of intensity, which is being extracted by keeping $t = 0$ and $r = 0$ condition, respectively, at three power levels (below P_{cr}, at P_{cr} and just above P_{cr}).

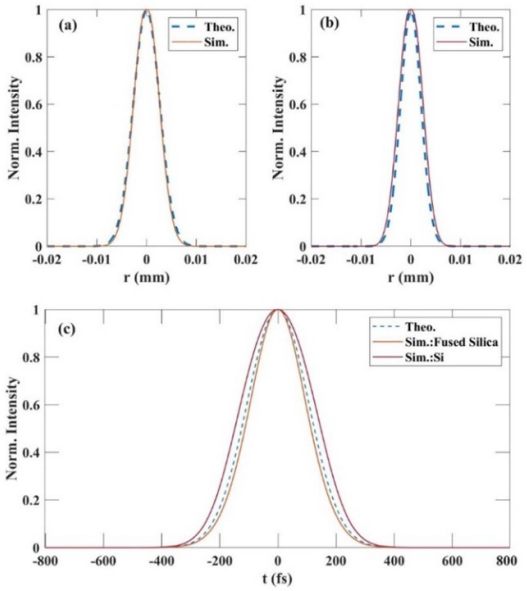

Figure 4. Spatial profile of laser pulse in terms of intensity for FS (a) and Si (b). (c) Temporal laser pulse profile of materials. Solid line is simulated data and dotted line is theoretical data for the linear case. All simulated data are extracted at the geometrical focal point for each material.

Previously, from figure 3(a), the deviation of maximum delivered fluence versus linear theoretical (theo.) case at focus is observed at $P_{in}/P_{cr} = 0.25$ and the 0.1 case for FS and Si, respectively. In these specific cases, we have checked both spatial and temporal pulse profile evolution of our simulated pulses at focus, which are being normalized. As shown in figure 4(a), the radial part of our simulated pulse nearly overlaps with the theoretical one (focal spot size ($1/e^2$) $w_0 = 5.2$ μm in the simulation (sim.) case and 5.3 μm in theoretical (theo.) case for FS, whereas for Si, it is stretched 24% more in the radial part compared to the theoretical case, which is shown in figure 4(b). Whereas, in the case of the temporal part, the pulse duration is compressed by a factor of 0.86 times our given pulse duration (τ_0) in the FS case, as shown in figure 4(c). However, in Si, the pulse duration is stretched to a factor of $1.2\tau_0$. The above spatio-temporal compression effect in the case of FS helps to increase the intensity value at focus with respect to the theoretical case, which is observed in our delivered fluence profile in the $P_{in}/P_{cr} = 0.25$ case (as discussed before in figure 3(a)). A similar kind of compression effect in the temporal part of the pulse is also present in a previous report [44] in the FS case. Whereas, for the Si case, we have observed a stretching effect, which in turn reduces fluence delivery to focus, compared to the theoretical one in the $P_{in}/P_{cr} = 0.1$ case (as discussed before in figure 3(a)). This long dispersed beam will help to reduce the fluence delivery condition at the focal point in the case of Si.

For the critical ($P_{in}/P_{cr} = 1$) case, the radius of the pulse profile is significantly compressed, where simulated spot size is 50% narrower compared to the theoretical one, as shown in figure 5(a). Whereas for the Si case, there is no significant stretching where the spot size is increased by just 4% compared to the theoretical case, as shown in figure 5(b). Simultaneously, strong compression has been observed in the case of FS, where τ_0 is reduced to 40% for the temporal case of our simulated pulse profile, as shown in figure 5(c). In the Si case, it is stretched to $1.6\tau_0$. Overall, there is a strong compression effect in both spatio-temporal profiles of laser pulses observed in FS in the self-focusing case because of which it can create a strong local hot-spot in fluence delivery (as shown in figure 1(b)). Whereas, for Si, the strong stretching of the pulse profile does not add any strong asymmetries to the propagation aspect where we have not observed any nonlinear effects such as beam collapse, filamentation, etc (as shown in figure 2(b)).

In the strongly nonlinear ($P_{in}/P_{cr} = 2$) case, we have observed the pulse-splitting behavior in the radial direction for FS, as shown in figure 6(a). Whereas, for Si, the spot size is stretched to only 4%, as shown in figure 6(b). Similarly, in the temporal case, the splitting of the two pulses is clearly observable for the FS case, as shown in figure 6(c) where the first and second pulse are compressed to 30 and 90 fs, respectively, having a separation of 180 fs. On the other hand, the dispersed pulse is nearly twice that of our given pulse duration in the Si case due to the addition of two long dispersed pulses where splitting is not initiated. By analyzing the above points at above P_{cr} conditions, we show that pulse splitting in the spatio-temporal direction of the FS is the dominant phenomenon for strong self-focusing features. However, for Si, the above prominent pulse-splitting feature at focus is not observable even if P_{cr} is attained. Therefore, a clear framework of our simulated pulses' evolution along both radial and temporal parts at different Z points needs to be verified for

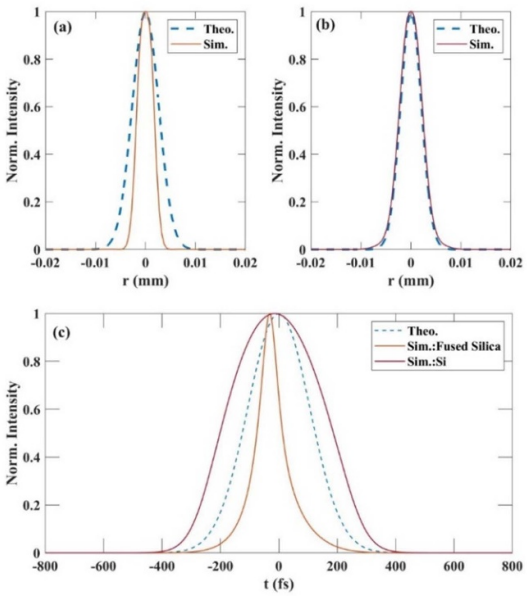

Figure 5. Spatial profile of laser pulse in terms of intensity for FS (a) and Si (b). (c) Temporal laser pulse profile of materials. All these profiles have been extracted from the $P_{in}/P_{cr} = 1$ case for both materials.

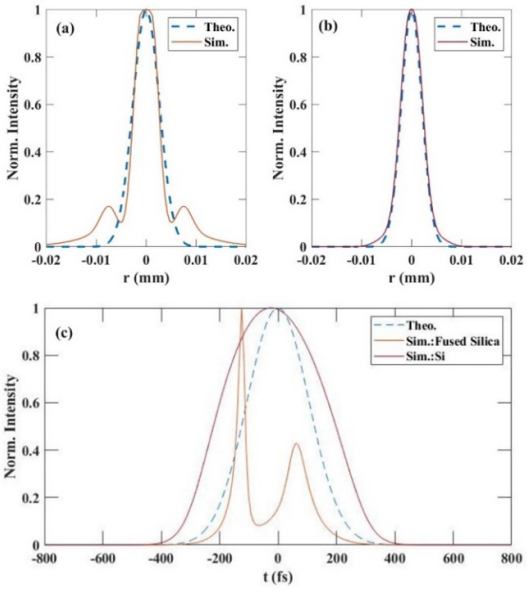

Figure 6. Spatial pulse profile in terms of normalized intensity for fused silica (a) and Si (b) for above-critical case ($P_{in}/P_{cr} = 2$). (c) Temporal laser pulse profile of materials at the above stated power level.

both materials to understand this complex behavior of pulse slitting in the above nonlinear regime ($P_{in}/P_{cr} = 2$).

3.4. Pulse splitting in FS and Si

As a result, the simulated spatial and temporal pulse profile evolutions (in normalized form) are as shown in figure 7 at different Z points at just above the critical case ($2P_{cr}$) for both materials. In figure 7(a), pulse splitting in the radial direction is already being initiated at the pre-focal point (starting from $Z = 2.8$ mm) in the FS case. Simultaneously, the temporal profile is compressed to 40% at the same Z point, as shown in figure 7(b). Since we use very low effective NA, the laser pulse travels a longer distance to reach focus. When self-focusing occurs, the beam collapse is already initiated at the pre-focal position, where it is further arrested by the splitting of pulses in both the spatial and temporal domains [44]. During the catastrophic collapse of a laser beam, there is a significant modulation instability of a plane wave [49], because of which a single peak pulse splits into sub pulses in both spatial and temporal domains. The above phenomenon has

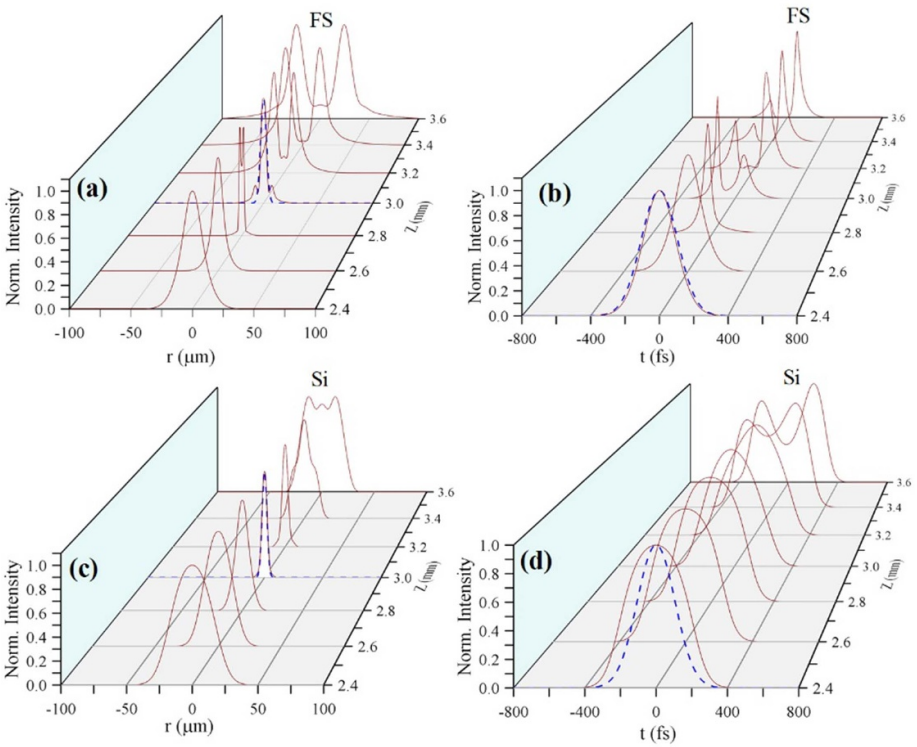

Figure 7. (a) Radial (r) and (b) temporal (t) pulse profile evolution along Z (propagation axis) in terms of normalized intensity for FS. Similar cases are followed in the case of Si considering the respective (c) spatial and (d) temporal pulse profile evolution. All the above simulated profiles have been extracted at the above-critical case where $P_{in}/P_{cr} = 2$. Dotted lines represent the theoretical radial (at focal plane $Z = 3$ mm) and temporal beam profile (at pre-focal). Here, this simulation group velocity dispersion's contribution to temporal dispersion of our simulated pulse profile is negligible for both materials.

already been observed both experimentally and numerically inside the FS in previous reports [50, 51] for femtosecond pulses. Thus, spatial pulse splitting and temporal compression effects at the pre-focal distance create a strong local hot-spot before the focal plane, resembling the behavior of filamentation as observed before (please check figure 1(c)) in FS. This has been further verified by checking the absolute intensity value at the respective Z point where the maximum intensity is already more than three times higher than the theoretical one in both radial and temporal cases (please see figures S3 (a) and (b) in the SM). Later, after the focal point Z_0, the pulse splits into two parts in both radial and temporal direction. However, if we check the delivered intensity cases after the focal point ($Z = 3$ mm), although pulse splitting is present in this case, the maximum intensity is already one order lower than that in the pre-focal case $Z = 2.8$ mm (please see figures S3 (a) and (b) in the SM) so that the value of the delivered fluence at the post focal positions is not so significant in the propagation aspect.

In the Si case, from figures 7(c) and (d) there is no such splitting in both the radial and temporal parts of the pulse till the focusing depth ($Z = 3$ mm). Since a strongly dispersed beam is present in the time domain (as discussed before in section 3.3) propagating inside the medium, it delivers reduced fluence at focus (as shown in figure 2(c)). We further verified this argument by checking the on-axis intensity of pulses at different propagation positions (please see figures S3(c) and (d) in the SM) where the maximum intensity at geometrical focus is nearly one order below the theoretical case, which resembles the fluence delivery condition at $P_{in}/P_{cr} = 2$ (as shown in figure 2(c)). In our simulations, we have verified that the contribution of group velocity dispersion (GVD) to the above temporal dispersion is negligible. Our assumption is that terms other than GVD in equation 1 could influence this phenomenon. The long stretching near the focal region can also arise as an initiation mechanism for pulse splitting along the temporal part. This is because in later depth pulse splitting is prominent after the focal region (here starting from $Z = 3.2$ mm), which is already out of depth of focus. However, rigorous numerical study is further required in the future to prove these points. We also show that there is no asymmetric distribution of fluence delivery conditions even if the above-critical self-focusing condition (as shown in figure 1(f)) is achieved. We further verified this justification by checking the absolute intensity of our simulated beam in both radial and temporal domains after focus (please see the on-axis intensity distribution profiles of figures S3(c) and (d) in the SM) where the

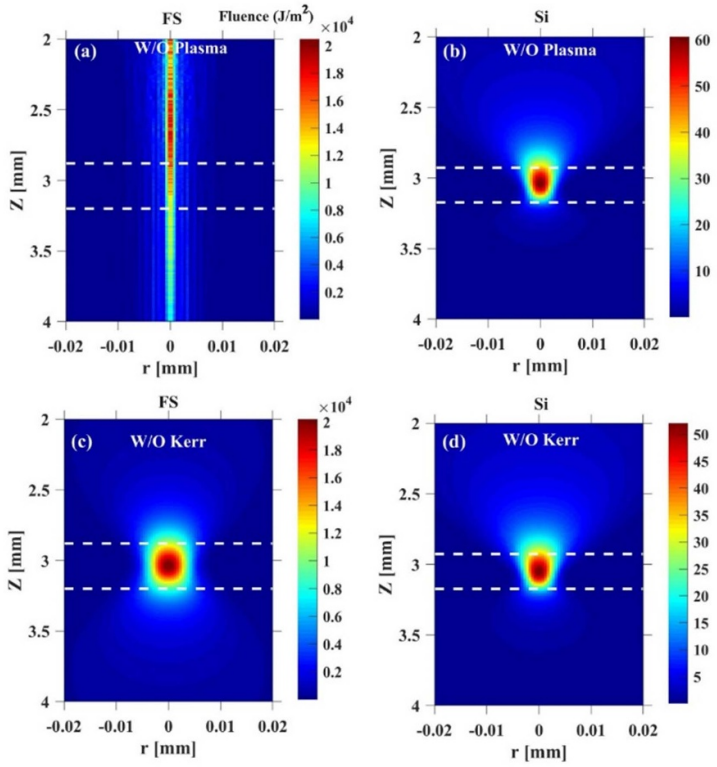

Figure 8. Simulated 2D fluence plot versus the radial part of the pulse profile without the plasma term in FS (a) and Si (b). Similar profiles have been obtained under no Kerr term condition in the case of FS (c) and Si (d). All the profiles have been simulated at above-critical power level ($P_{in}/P_{cr} = 2$).

maximum intensity value at post focal approaching the background, which is already 3–7 times below the maximum intensity in the focal region.

Through the above discussion, it can be seen that the propagation-induced nonlinearities (self-focusing, filamentation, etc) are more prone to FS compared to Si at the above-critical self-focusing condition. So, what is the origin of these nonlinearities inside dielectrics like FS in this case that makes it an ideal candidate to create such strong filamentation and why is Si not so effective in this given focusing condition?

3.5. Importance of plasma and the Kerr term in laser propagation

To address this issue, two cases are taken where we have omitted plasma and the Kerr term (terms affecting the nonlinear effects), respectively, in the above-critical case ($2P_{cr}$) and checked the influence of these omissions on the laser propagation condition in equation (1). From figure 8(a), it can be seen that there are many local hot spots, which are being generated in the pre-focal region inside the FS where we switch off the plasma term. The above distribution of propagation suggests that filamentation is dominant where the Kerr term is active in the propagation equation. In contrast, there is no such nonlinear process (self-focusing, plasma-defocusing, etc) involved in the Si case, as shown in figure 8(b) where fluence is localized inside depth of focus. As a result, the omission of the plasma term dominates the propagation aspect for FS compared to Si.

Similarly, when we de-activate the Kerr term in equation 2 for FS, the fluence profile is symmetric where the maximum fluence is delivered to geometrical focus Z_0, as shown in figure 8(c). Whereas, for the Si case, we have observed a radially dispersed beam at the pre-focal position where localization of the maximum fluence is attained near Z_0. Along with that, the profiles shown in figure 8 suggest that when there is strong self-focusing, and we expect a splitting mechanism in the pulse profile (as explained before in section 3.3), which is prominent in FS, whereas, for Si, it is absent. This is further verified by checking the temporal part of the simulated pulse where multi-pulse splitting is happening in the FS, whereas strong dispersion is observed in Si (please see figure S4 in the SM).

Now, one important question arises. Is filamentation possible in the case of Si if we further increase the power level a few orders higher than that of critical power under this given focusing condition ($NA_{eff} = 0.11$)? To answer the above, we have further increased the power level to $100P_{cr}$ and $1000P_{cr}$, respectively, and checked the fluence delivery conditions by referring to equation (1) where all terms are active. From figures 9(a) and (b), even if P_{in} is increased by a few orders, it does not influence the arising

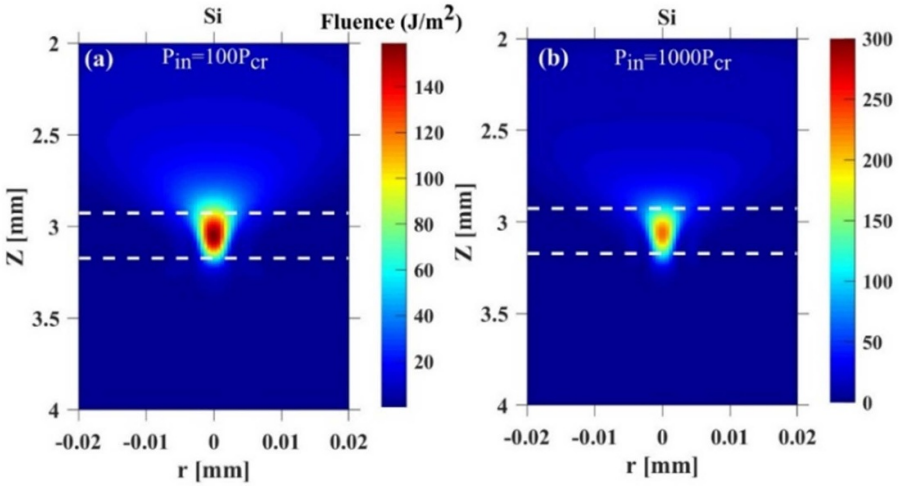

Figure 9. 2D-simulated laser propagation profile in terms of delivered fluence at two power levels, i.e. $P_{in} = 100P_{cr}$ (a) and $P_{in} = 1000P_{cr}$ (b). These simulations are performed based on equation (1) where all terms are active.

filamentation condition since the beam is delivered near the focal position Z_0 with an enhanced value. In practice, we could expect strong plasma deposition near the surface, which could ablate the material's surface (where the input power level is above the laser-induced damage threshold of the surface [52]) at these higher power levels for Si. Further experimental verification is needed to validate the above.

However, both plasma and Kerr terms effectively contribute to the localization of the beam at these higher power levels for Si. We conclude that until and unless there is no strong contribution of one nonlinear term (here Kerr term for FS) compared to the other term (here Plasma term for FS) in overall propagation condition, we cannot expect strong nonlinearities such as self-focusing, plasma-defocusing, etc, inside any material. This gives a simple guideline for understanding the complex processes involved in laser processing of these transparent materials.

4. Conclusion

In summary, we have numerically investigated the laser propagation conditions in FS and Si, respectively, under similar focusing conditions. We have observed a strong possible self-focusing effect for the FS case when the input power level is approaching the critical power. Whereas for Si, it does not influence laser propagation. Similar behavior persists in carrier density delivery conditions for both materials. The origin of these conditions is further verified by checking the spatio-temporal pulse profile evolution at above-critical conditions. In this case, strong compression of the spatial and temporal part of our simulated pulse with the splitting pulse at focus addresses the above phenomenon, resulting in the initiation of strong localized hot spots in the FS. Whereas, in Si, there is a strong dispersion in the temporal part of our pulse that may play a role in creating localized symmetric fluence delivery even if critical power is attained. We have further investigated the influence of the Kerr and plasma terms on propagation conditions in this case for both materials. One conclusion can be made that the origin of filamentation in the FS can arise from the strong contribution of the omission of the plasma term compared to the Kerr term where the beam collapse is initiated at high electric field. For Si, there is an equivalent contribution of both plasma and Kerr terms with a long temporally dispersed beam that plays a role in propagating reduced localized fluence delivery near the focus region where filamentation is absent.

Data availability statement

The data cannot be made publicly available upon publication because no suitable repository exists for hosting data in this field of study. The data that support the findings of this study are available upon reasonable request from the authors.

Acknowledgment

The authors would like to thank Professor Shuting Lei (Kansas State University) for fruitful discussion of the results that have been presented in this report. Funding support from the National Science Foundation under Award Number ECCS 2129006 is acknowledged.

Conflict of interest

The authors declare no conflicts of interest.

Funding

National Science Foundation (NSF) ECCS 2129006.

ORCID iD

Amlan Das https://orcid.org/0000-0002-1804-3717

References

[1] Itoh K, Watanabe W, Nolte S and Schaffer C B 2006 *MRS Bull.* **31** 620–5
[2] Gattass R and Mazur E 2008 *Nat. Photon.* **2** 219–25
[3] Selimis A, Mironov V and Farsari M 2015 *Microelectron. Eng.* **132** 83–89
[4] Stoian R 2020 *Appl. Phys.* A **126** 1–30
[5] Liao Y, Song J, Li E, Luo Y, Shen Y, Chen D, Cheng Y, Xu Z, Sugioka K and Midorikawa K 2012 *Lab Chip.* **12** 746
[6] Deubel M, von Freymann G, Wegener M, Pereira S, Busch K and Soukoulis C M 2004 *Nat. Mater.* **3** 444–7
[7] Sugioka K, Gu B and Holmes A 2007 *MRS Bull.* **32** 47–54
[8] Eaton S M, Cerullo G and Osellame R 2012 Fundamentals of femtosecond laser modification of bulk dielectrics *Femtosecond Laser Micromachining. Topics in Applied Physics* vol 123, ed R Osellame, G Cerullo and R Ramponi ed (Springer)
[9] Juodkazis S, Nishimura K and Misawa H 2007 *Appl. Surf. Sci.* **253** 6539–44
[10] Vartapetov S K, Ganin D V, Lapshin K E and Obidin A Z 2015 *Quantum Electron.* **45** 725–30
[11] Zhao J, Zhang C, Liu F and Cheng G J 2021 *Carbon* **175** 352–63
[12] Zhou S, Shen L, Wang F, Li Y, Zhang H, Wang S and Zhou S 2022 *Opt. Laser Technol.* **147** 107687
[13] Das A, Wang A, Utéza O and Grojo D 2022 *Opt. Express* **30** 39101–10
[14] Zhang H, Ho S, Eaton S M, Li J and Herman P R 2008 *Opt. Express* **16** 14015–23
[15] Bhardwaj V R, Corkum P B, Rayner D M, Hnatovsky C, Simova E and Taylor R S 2004 *Opt. Lett.* **29** 1312–4
[16] He S *et al* 2012 *J. Micromech. Microeng.* **22** 105017
[17] Tokel O *et al* 2017 *Nat. Photon.* **11** 639–45
[18] Chambonneau M, Li Q, Chanal M, Sanner N and Grojo D 2016 *Opt. Lett.* **41** 4875–8
[19] Saltik A and Tokel O 2024 *Opt. Lett.* **49** 49–52
[20] Tamaki T, Watanabe W, Nagai H, Yoshida M, Nishii J and Itoh K 2006 *Opt. Express* **14** 6971–80
[21] Little D J, Ams M, Dekker P, Marshall G D, Dawes J M and Withford M J 2008 *Opt. Express* **16** 20029–37
[22] Taylor R, Hnatovsky C and Simova E 2008 *Laser Photon. Rev.* **2** 26–46
[23] Yao Q, Song J, Yin W, Shi H, Yao H, Su Z and Dai Y 2023 *J. Appl. Phys.* **56** 265101
[24] Kononenko V V, Konov V V and Dianov E M 2012 *Opt. Lett.* **37** 3369
[25] Chanal M, Fedorov V Y, Chambonneau M, Clady R, Tzortzakis S and Grojo D 2017 *Nat. Commun.* **8** 1–6
[26] Das A, Wang A, Uteza O and Grojo D 2020 *Opt. Express* **28** 26623–35
[27] Verburg P C, Römer G R B E and Veld A J 2014 *Opt. Express* **22** 21958–71
[28] Chambonneau M, Lavoute L, Gaponov D, Fedorov V Y, Hideur A, Février S, Tzortzakis S, Utéza O and Grojo D 2019 *Phys. Rev. Appl.* **12** 024009
[29] Wang A, Das A and Grojo D 2020 *Research* **2020** 1–11
[30] Wang A, Das A and Grojo D 2020 *Phys. Rev. Res.* **2** 033023
[31] Peterson J R 2020 SNOPROP: a solver for nonlinear optical propagation *Zenodo* (https://doi.org/10.5281/zenodo.3908609)
[32] Sudrie L, Couairon A, Franco M, Lamouroux B, Prade B, Tzortzakis S and Mysyrowicz A 2002 *Phys. Rev. Lett.* **89** 186601
[33] Morgan C G 1975 *Rep. Prog. Phys.* **38** 621–65
[34] Sprangle P, Peñano J R and Hafizi B 2002 *Phys. Rev.* E **66** 046418
[35] Malitson I H 1965 *J. Opt. Soc. Am.* **55** 1205–9
[36] Li H H 1980 *J. Phys. Chem. Ref. Data* **9** 561–658
[37] Couairon A, Sudrie L, Franco M, Prade B and Mysyrowicz A 2005 *Phys. Rev.* B **71** 125435
[38] Bristow A D, Rotenberg N and van Driel H M 2007 *Appl. Phys. Lett.* **90** 191104
[39] Salzberg C D and Villa J J 1957 *J. Opt. Soc. Am.* **47** 244–6
[40] Chambonneau M *et al* 2021 *Phys. Rev. Res.* **3** 043037
[41] Gedeon V, Gedeon S, Lazur V, Nagy E, Zatsarinny O and Bartschat K 2012 *Phys. Rev.* A **85** 022711
[42] Marburger J H 1975 *Prog. Quantum Electron.* **4** 35–110
[43] Couairon A and Mysyrowicz A 2007 *Phys. Rep.* **441** 47–189
[44] Wu Z, Jiang H, Sun Q, Yang H and Gong Q 2003 *Phys. Rev.* A **68** 063820
[45] Saliminia A, Nguyen N T, Chin S L and Vallée R 2004 *Opt. Commun.* **241** 529–38
[46] Zhang L, Xi T, Hao Z and Lin J 2016 *J. Phys. D: Appl. Phys.* **49** 115201

[47] Mareev E I, Lvov K V, Rumiantsev B V, Migal E A, Novikov I D, Stremoukhov S Y and Potemkin F V 2020 *Laser Phys. Lett.* **17** 015402
[48] Mareev E, Obydennov N and Potemkin F 2023 *Photonics* **10** 380
[49] Zharova N A, Litvak A G, Petrova T A, Sergeev A M and Yunakovskii A D 1986 *JETP Lett.* **44** 13
[50] Zozulya Alex A *et al* 1999 *Phys. Rev. Lett.* **82** 1430
[51] Tzortzakis S, Sudie L, Franco M, Prade B, Mysyrowicz A, Couairon A and Berge L 2001 *Phys. Rev. Lett.* **87** 213902
[52] Tran D V, Zheng H Y, Lam Y C, Murukeshan V M, Chai J C and Hardt D E 2005 *Opt. Lasers Eng.* **43** 977–86